OPEN

NPG Asia Materials (2014) 6, e140; doi:10.1038/am.2014.100

www.nature.com/am

ORIGINAL ARTICLE

MnO_x/carbon nanotube/reduced graphene oxide nanohybrids as high-performance supercapacitor electrodes

Zhao Jun Han[1], Dong Han Seo[1,2], Samuel Yick[1,2], Jun Hong Chen[3] and Kostya (Ken) Ostrikov[1,2,4]

Nanohybrids consisting of both carbon and pseudocapacitive metal oxides are promising as high-performance electrodes to meet the key energy and power requirements of supercapacitors. However, the development of high-performance nanohybrids with controllable size, density, composition and morphology remains a formidable challenge. Here, we present a simple and robust approach to integrating manganese oxide (MnO_x) nanoparticles onto flexible graphite paper using an ultrathin carbon nanotube/reduced graphene oxide (CNT/RGO) supporting layer. Supercapacitor electrodes employing the MnO_x/CNT/RGO nanohybrids without any conductive additives or binders yield a specific capacitance of 1070 F g^{-1} at 10 mV s^{-1}, which is among the highest values reported for a range of hybrid structures and is close to the theoretical capacity of MnO_x. Moreover, atmospheric-pressure plasmas are used to functionalize the CNT/RGO supporting layer to improve the adhesion of MnO_x nanoparticles, which results in theimproved cycling stability of the nanohybrid electrodes. These results provide information for the utilization of nanohybrids and plasma-related effects to synergistically enhance the performance of supercapacitors and may create new opportunities in areas such as catalysts, photosynthesis and electrochemical sensors.

NPG Asia Materials (2014) **6**, e140; doi:10.1038/am.2014.100; published online 31 October 2014

INTRODUCTION

Supercapacitors are promising energy storage systems for diverse applications such as portable electronics, roll-up displays, hybrid electric vehicles, self-powered sensors, artificial muscles and biomedical implants.[1,2] The performance of supercapacitors fills the gap between batteries and conventional electrolytic capacitors, with such advantages as fast dynamic response, high power density, high rate capability, safe operation and long lifespan. The most common materials for current supercapacitor electrodes are high-surface-area carbon-based nanostructures, including activated carbons, porous/templated graphite, carbon nanotubes (CNTs) and graphene.[3–6] However, the relatively low specific capacitance and energy density of these carbon-based electrodes have so far hampered their widespread applications in real devices.

To address this challenge, hybrid materials that can synergistically combine the attributes of both carbon and pseudocapacitive materials such as metal oxides and conductive polymers have been actively pursued.[7–9] Pseudocapacitive materials store electrochemical energy in a similar manner as carbon-based materials but have a specific capacitance that is usually one order of magnitude larger. Among various pseudocapacitive materials, manganese oxides (MnO_x) have attracted the strongest interest because of their natural abundance, low cost and environmental friendliness.[10] Numerous studies have reported the hybrid structures of carbon materials with electrochemically active manganese oxide (MnO_x), most commonly MnO_2.[7] However, the maximum specific capacitance of MnO_2 in these reports remains low, at approximately 300–400 F g^{-1}, and the capacitance of overall hybrids is even lower, typically $<$200 F g^{-1};[11] MnO_2 still displays low electrical conductivity, limited stability and poor integration in hybrid electrode systems.

Mn can assume multiple oxidation states (Mn^{2+}, Mn^{3+} and Mn^{4+}) and diverse phases during both oxidation and reduction processes. According to the Pourbaix diagram, Mn_2O_3, Mn_3O_4 and MnO_2 can all be formed from a Mn^{2+} salt solution at room temperature.[12] Compared to single-phased MnO_2, MnO_x compounds (i.e., Mn atoms with multiple oxidation states and phases) usually contain both donor and acceptor sites in their microstructures as well as defects and mismatch induced by different phases, which can enable a higher charge storage capacity that is beneficial for supercapacitor applications.[13] However, despite a few examples of MnO_x reported recently,[14] most previous studies simply denoted the synthesized Mn oxides as MnO_2 with few or no structural investigations.[15–17] The integration of MnO_x into supercapacitor electrodes with binders is also challenging because of the non-uniform particle size, poor electrical conductivity and structural instability of MnO_x. In addition, MnO_x was mainly synthesized by methods involving hazardous chemicals,

[1]Industrial Innovation Program, CSIRO Manufacturing Flagship, Lindfield, New South Wales, Australia; [2]School of Physics, The University of Sydney, Sydney, New South Wales, Australia; [3]Department of Mechanical Engineering, University of Wisconsin-Milwaukee, Milwaukee, Wisconsin, USA and [4]Institute for Future Environments, School of Chemistry, Physics and Mechanical Engineering, Queensland University of Technology, Brisbane, Queensland, Australia
Correspondence: Professor K Ostrikov or Dr ZJ Han, CSIRO Manufacturing Flagship, P.O. Box 218, Bradfield Road, Lindfield, New South Wales 2070, Australia.
E-mail: kostya.ostrikov@csiro.au or zhaojun.han@csiro.au
Received 26 May 2014; revised 10 September 2014; accepted 11 September 2014

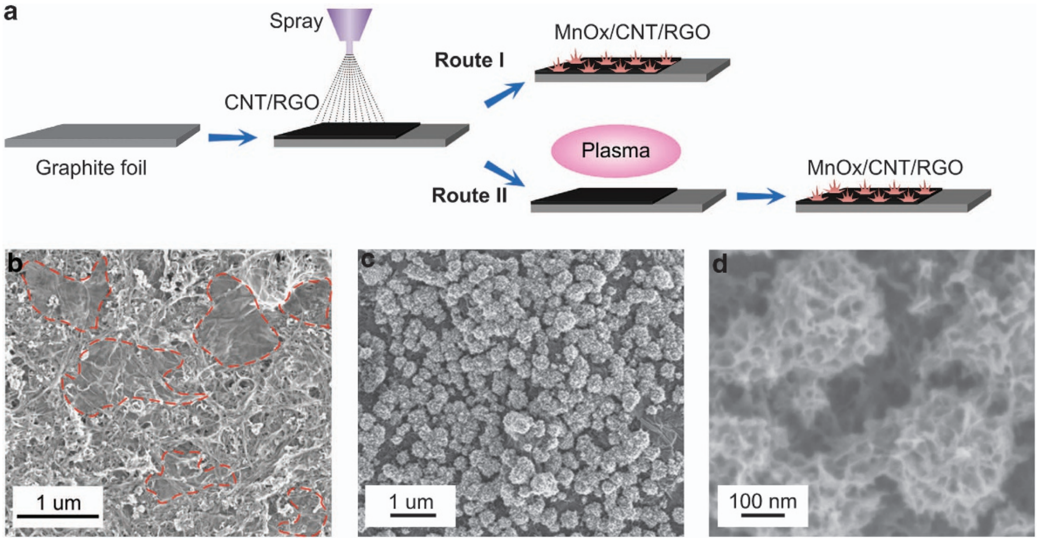

Figure 1 (**a**) Schematics for MnO$_x$/CNT/RGO nanohybrid fabrication via Routes I and II. Route II includes a plasma functionalization step prior to MnO$_x$ deposition. (**b**) SEM image of the CNT/RGO supporting layer, with RGO highlighted by dotted lines. (**c**) Low- and (**d**) high-magnification SEM images of MnO$_x$ nanoparticles deposited on a CNT/RGO layer.

strong acids and high-temperature thermal annealing, with the controllability, scalability and reliability of these methods remaining unclear. Therefore, control of the size, morphology and density of MnO$_x$ in a simple and environmentally benign way is highly desirable to realize the true potential of MnO$_x$ in energy storage devices.

Here, we present a robust approach to integrating a high density of MnO$_x$ nanoparticles onto flexible graphite paper using an ultrathin CNT and reduced graphene oxide (CNT/RGO) layer as the supporting layer. The ultrathin CNT/RGO supporting layer not only enables good electrical conductivity by forming web-like percolating networks but also improves the efficiency of MnO$_x$ deposition. The electrodeposited MnO$_x$ nanoparticles have a porous nanostructure and a narrow particle size distribution. Supercapacitor electrodes utilizing this MnO$_x$/CNT/RGO nanohybrid demonstrate good charge transfer conductance and high specific capacitance of 1070 F g^{-1}. This specific capacitance is substantially larger than the values (300–400 F g^{-1}) commonly obtained from MnO$_2$ electrode material with similar thickness and mass loading. Moreover, atmospheric-pressure dielectric-barrier discharge (DBD) plasmas are used to functionalize the CNT/RGO supporting layer prior to MnO$_x$ deposition. The resulting nanohybrid displays improved cycling stability without compromising specific capacitance. These results demonstrate the promise of the synergistic use of carbon nanomaterials and plasma-related effects in the development of high-performance energy storage devices and may create new directions for functional devices in the fields of catalysis, photosynthesis and electrochemical sensing.

MATERIALS AND METHODS

Preparation of MnO$_x$/CNT/RGO nanohybrids

First, 50 mg CNTs (~1.0 nm diameter; Sigma, Sydney, Australia) and 50 mg RGO monolayer (0.7–1.2 nm thick; NanoInnova Technologies, Madrid, Spain) were dissolved in 100 ml *N*-methyl-2-pyrrolidone. A stable solution was obtained after horn sonication (Sonics VCX130, John Morris Scientific, Sydney, Australia) at 100 W for 30 min. Graphite foil (0.25 mm thick; Alfa Aesar, Ward Hill, MA, USA) was used as the flexible substrate. An ultrathin layer of CNT/RGO was then formed on the graphite foil by spray coating, followed by annealing at 80 °C on a hot plate in air.

MnO$_x$ nanoparticles were synthesized by galvanostatic electrodeposition in a two-electrode cell configuration, with the CNT/RGO-coated graphite foil as the working electrode, a Pt plate as the counter/reference electrode and MnSO$_4$ as the precursor solution, as shown by Route I in Figure 1a. MnO$_x$ nanoparticles were deposited at a constant current of 1 mA cm^{-2} for 0.5–20 min in 0.2 M MnSO$_4$ aqueous solution. The MnO$_x$/CNT/RGO/ electrode was then washed with ethanol and water and dried at 80 °C for 3 h in air. The mass of MnO$_x$ nanoparticles was measured by an ultrasensitive microbalance with a sensitivity of 0.1 μg (Mettler Toledo UMT2, Port Melbourne, VIC, Australia). The loading of MnO$_x$ was 30 ± 5 μg and ~ 300 μg for 2 and 20 min deposition, respectively. Finally, supercapacitor electrodes were fabricated from the CNT/RGO/MnO$_x$ hybrid structure without any conductive additives or polymeric binders.

To improve the stability of MnO$_x$ nanoparticles in the nanohybrid, an atmospheric-pressure DBD plasma (see Supplementary Figure S1) was used to functionalize the ultrathin CNT/RGO layer prior to MnO$_x$ deposition, as illustrated by Route II in Figure 1a. The plasma discharge was powered by a high-frequency pulse generator (Corona Lab CTP-2000K, Nanjing, China) at 100 V and 0.16 A (i.e., at power of ~ 16 W). Helium was used as a working gas. The CNT/RGO layer on graphite foil was treated for 5 min, followed by the electrodeposition of MnO$_x$ nanoparticles as described above.

Electrochemical measurements

The electrochemical performance of MnO$_x$/CNT/RGO hybrid electrodes was conducted in a three-electrode cell configuration using a potentiostat/galvanostat (Bio-Logic VSP 300, Claix, France). The nanohybrid was used as the working electrode, with Ag/AgCl as the reference electrode, a Pt plate as the counter electrode and 1 M Na$_2$SO$_4$ aqueous solution as the neutral electrolyte. Cyclic voltammetry (CV) was performed at scan rates from 10 to 500 mV s^{-1}, and galvanostatic charge/discharge measurements were conducted at current densities from 150 to 800 μA cm^{-2}. Electrochemical impedance spectroscopy using a 10 mV sinusoidal signal was measured at open-circuit voltage, with frequency scanned from 0.01 Hz to 1 MHz. Specific capacitance based on the CV curves was calculated by $C_s = \int IdV/mvV$, where I is the current, V is the potential window, m is the mass loading of MnO$_x$ and v is the scan rate, while specific capacitance based on the charge/discharge curves was calculated by $C_s = i/(-dV/dt)$, where i is the discharge current and dV/dt is the slope of the discharge curve. Capacitance contributed from the graphite foil was subtracted in both cases.

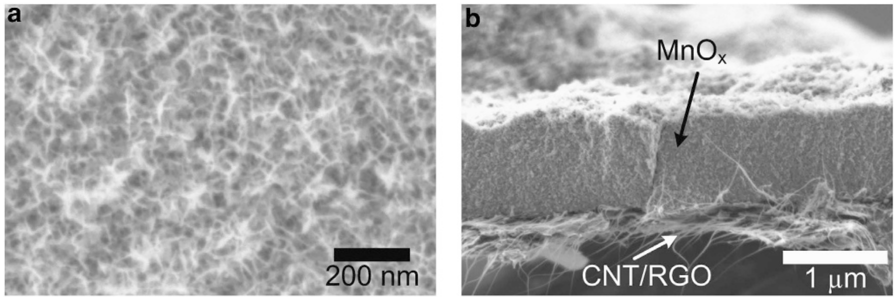

Figure 2 (**a**) Top-view and (**b**) cross-sectional SEM images of MnO_x nanoparticles with a thickness of approximately 1.2 μm deposited on a CNT/RGO supporting layer.

Materials characterization

Scanning electron microscopy equipped with energy-dispersive X-ray spectroscopy was performed using a Zeiss Auriga microscope (Carl Zeiss, Sydney, Australia) operating at 1 keV electron beam energy with an InLens detector. Transmission electron microscopy (JEOL 2100, JEOL, Sydney, Australia) was operated at an electron beam energy of 200 keV. Samples for transmission electron microscopy characterization were prepared by shaving the surface material using a scalpel, ultrasonicating in ethanol, dropping onto holey carbon-coated copper grids and drying naturally in air. Raman spectroscopy utilized a Renishaw *inVia* spectroscope (Renishaw, Sandringham, VIC, Australia) with laser excitation of 514 nm and a spot of ~1 μm^2. Furthermore, X-ray photoelectron spectroscopy (XPS) used a SAGE 150 SPECS system (SPECS GmbH, Berlin, Germany) with a Mg *K*α source at 1253.6 eV. Peak analyses were performed using CasaXPS (Casa Software, http://www.casaxps.com).

RESULTS AND DISCUSSION

Fabrication of MnO_x/CNT/RGO nanohybrids

The morphology of the sprayed CNT/RGO supporting layer on the graphite foil and the deposited MnO_x nanoparticles are shown in Figures 1b–d. Entangled CNTs and RGO with a thickness of 10–20 nm cover the entire graphite foil (Figure 1b). After galvanostatic deposition, flower-shaped MnO_x nanoparticles grow on the CNT/RGO supporting layer, with sizes ranging from 100 to 200 nm (Figure 1c). MnO_x nanoparticles form a near-continuous monolayer with a highly porous structure after only 2 min deposition (Figure 1d). These nanoparticles firmly attach to the CNT/RGO supporting layer, thereby avoiding the polymeric binders commonly used in the integration of supercapacitor electrodes. The mass loading of MnO_x nanoparticles was ~30 μg. Moreover, energy-dispersive X-ray spectroscopy measurements indicate that the molar ratio of O and Mn atoms is approximately 1.38 (see Supplementary Figure S2), suggesting that MnO_x most likely consists of Mn_3O_4 and Mn_2O_3. The formation of a mixed-valent compound rather than single-phased MnO_2 is attributed to oxygen deficiency in the electrodeposition process. Compared to pristine graphite foil, the CNT/RGO supporting layer not only increases the density of MnO_x nanoparticles but also leads to a smaller size and narrower size distribution (see Supplementary Figure S3).

Both CNT and RGO are promising candidates for the fabrication of electrical double-layer capacitor type supercapacitors.[3–5] However, the specific capacitance and energy density of electrical double-layer capacitor-type supercapacitors are still below the requirements of most real applications. In the current hybrid structure, the ultrathin CNT/RGO supporting layer promotes MnO_x electrodeposition and maintains strong electrical contact between the graphite foil and the electrochemically active but poorly conductive MnO_x nanoparticles.[8] The latter is apparent as CNTs form web-like conductive percolating networks and RGO further reduces the interfacial resistance in the percolating networks through its two-dimensional structure (Figure 1b).[18]

We have performed a series of experiments to control the structure of MnO_x nanoparticles. By reducing the $MnSO_4$ salt concentration, a broad particle size distribution is formed (see Supplementary Figure S4). At the present concentration of 0.2 M $MnSO_4$ and a constant current of 1 mA cm^{-2}, the voltage approaches a steady state of 2.2 V after ~100 s (see Supplementary Figure S5). With prolonged deposition at these conditions, we can readily deposit a thicker layer of MnO_x while maintaining the porous structure. As shown in Figure 2, a 1.2-μm-thick film with a mass loading of ~300 μg cm^{-2} is obtained after 20 min, indicating that the packing density of MnO_x increases proportionally with deposition time (scanning electron microscopy images of MnO_x deposited for 5 and 10 min are also shown in Supplementary Figure S6). Therefore, by combining CNTs and RGO in the supporting layer, the thickness and morphology of MnO_x nanoparticles can be effectively controlled.

Hybrid structures containing Mn oxides have been previously prepared by a number of methods, such as physical mixing, vacuum filtration, direct redox precipitation and hydrothermal processes.[19] Nevertheless, control of the size, density, morphology and thickness of Mn oxides remains a challenge. The galvanostatic electrodeposition method employed here is a simple and effective way to control the deposition of MnO_x nanoparticles and involves only hazard-free chemicals. The method also has such advantages as being single-step, environmental friendliness, reliability, scalability, low cost and versatility.

The chemical bonding states of MnO_x nanoparticles were analyzed in detail by XPS and Raman spectroscopy. The XPS survey scans of CNT/RGO and MnO_x/CNT/RGO are shown in Figure 3a, which clearly indicates the introduction of Mn atoms by the electrodeposition process. The C 1s spectra show similar carbon bonds in both samples (see Supplementary Figure S7), suggesting that the CNT/RGO supporting layer remains largely intact after MnO_x deposition. Figure 3b shows the O 1s spectrum of the CNT/RGO/MnO_x nanohybrid, in which three deconvoluted peaks can be assigned to the chemical bonds of Mn-O-Mn, Mn-O-H and H-O-H at binding energies (BE) of 529.8, 531 and 532 eV, respectively. This O 1s spectrum is typical for compounds with Mn ions in the 2+ or 3+ oxidation states.[20,21] The Mn 2p spectrum of CNT/RGO/MnO_x also shows two peaks at binding energies of ~654 and ~642 eV (Figure 3c), which can be attributed to the Mn $2p_{3/2}$ and Mn $2p_{1/2}$ spin-orbital doublets, respectively.[21] Moreover, the Mn 3s spectrum displays a splitting width of ~5.6 eV, implying the presence of Mn^{3+} and Mn^{2+} states (see Supplementary Figure S8).[20]

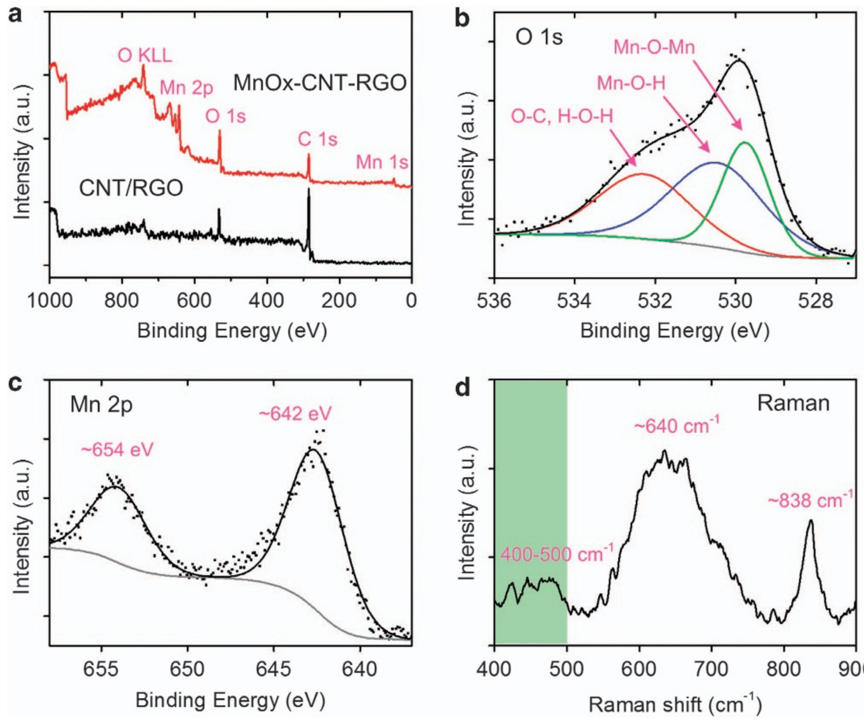

Figure 3 (**a**) XPS survey scans of CNT/RGO and MnO$_x$/CNT/RGO nanohybrid. (**b**) O 1s and (**c**) Mn 2p spectra of MnO$_x$/CNT/RGO nanohybrid. (**d**) Raman spectrum of MnO$_x$/CNT/RGO nanohybrid. The peak at ~838 cm^{-1} is from the vibrations in CNTs.

Raman spectroscopy was also used to analyze the MnO$_x$ structural features over large areas.[12] A Raman spectrum of the MnO$_x$/CNT/RGO is shown in Figure 3d, and the spectra of pristine graphite foil, CNT and RGO are shown in Supplementary Figure S9. The peak observed in Figure 3d at Raman shift of ~640 cm^{-1} can be attributed to the Mn-O stretching vibration in the basal plane of MnO$_6$ and/or the symmetric stretching vibration (Mn-O) of the MnO$_6$ group.[19] In particular, the broad peak at 550–750 cm^{-1} can be assigned to the δ-phase of the characteristic Mn$_3$O$_4$ Raman spectrum, while the peaks from 400 to 500 cm^{-1} are fingerprints of Mn$_2$O$_3$.[12,21] These peaks are broad, indicative of the small crystal sizes of MnO$_x$ nanoparticles that lack significant long-range order. These spectra thus corroborate that the MnO$_x$ is comprised of mainly Mn$_3$O$_4$ and Mn$_2$O$_3$ phases.

Figure 4 shows a transmission electron microscopy image of the MnO$_x$ nanoparticles. These flower-shaped nanoparticles firmly attach to the CNT/RGO supporting layer with multiple crystalline nano-domains, which can be assigned to different facets of the mixed-valent nanohybrid, such as the (111) plane of Mn$_2$O$_3$, (211) plane of Mn$_3$O$_4$, (101) plane of Mn$_3$O$_4$ and (002) plane of graphitic carbon.[22,23] In fact, a very recent report has described such flower-shaped MnO$_x$ nanoparticles to have α-Mn$_2$O$_3$ in the core and Mn$_3$O$_4$ Hausmannite in the branches.[14]

Electrochemical performance of MnO$_x$/CNT/RGO nanohybrid

When subjected to a potential sweep (0–0.8 V) in the presence of aqueous electrolyte during electrochemical tests, the initial MnO$_x$ nanoparticles may undergo oxidation to a higher valent state after the first few cycles (see Supplementary Figure S10). However, no significant morphological changes associated with the phase transformation to MnO$_2$ were observed, indicating that the oxidation of MnO$_2$ to a monolithic state is a gradual and long process. As a result, the defects and mismatch induced by different phases in the as-synthesized MnO$_x$ remain unchanged in the oxidation process.[14] The oxidation reactions are[12]

$$Mn_2O_3 + 3H_2O \rightarrow 2MnO_2 + 2H_3O^+ + 2e^-,$$

and

$$Mn_3O_4 + 6H_2O \rightarrow 3MnO_2 + 4H_3O^+ + 4e^-.$$

The charge storage capability of MnO$_2$ is then mainly determined by the surface adsorption of electrolyte cations and proton incorporation according to[24]

$$MnO_2 + Na^+ + H^+ + 2e^- \leftrightarrow MnOONaH.$$

These reactions are highly reversible only on the outmost surface layer in contact with the aqueous Na$_2$SO$_4$ electrolyte.[8,25] Thus, to best evaluate the ultimate charge storage capacity of MnO$_x$ nanoparticles, we conducted the electrochemical measurements of a monolayer of MnO$_x$ on the CNT/RGO supporting layer. Collected using a three-electrode test configuration, the CV curves of MnO$_x$/CNT/RGO in 1 M Na$_2$SO$_4$ aqueous electrolyte at scan rates of 10, 20 and 50 mV/s are shown in Figure 5a.

The CV curves show nearly symmetric quasi-rectangular shapes, similar to the electrical double-layer capacitor-type capacitive behavior, which is attributed to the successive multiple surface redox reactions of MnO$_x$, a charge storage mechanism that is different from that of most other metal oxides.[24] Therefore, smooth CV curves rather than distinct redox peaks are observed here. Additionally, the CNT/RGO supporting layer contributes negligible capacitance to the nanohybrid electrode, as suggested by comparing the CV curves of graphite foils with and without the CNT/RGO supporting layer (see Supplementary Figure S11). The thickness of CNT/RGO is very small (<20 nm), and the estimated mass is low (<2 μg). As a result, the CNT/RGO supporting layer in the nanohybrid acts similarly to a porous current collector, while the charge storage capacity is mainly determined by the MnO$_x$ nanoparticles.[26]

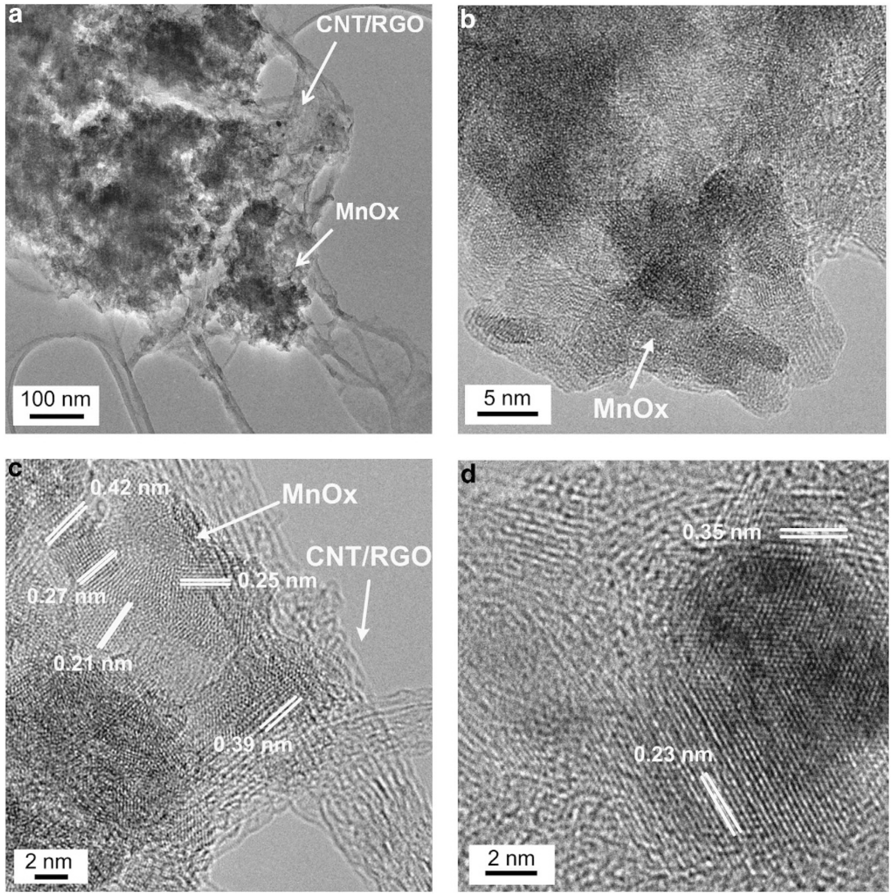

Figure 4 (**a**) Low- and (**b**–**d**) high-resolution transmission electron microscopy images of MnO_x/CNT/RGO nanohybrid, showing that MnO_x nanoparticles attached to the CNT/RGO supporting layer possess multiple crystalline nano-domains.

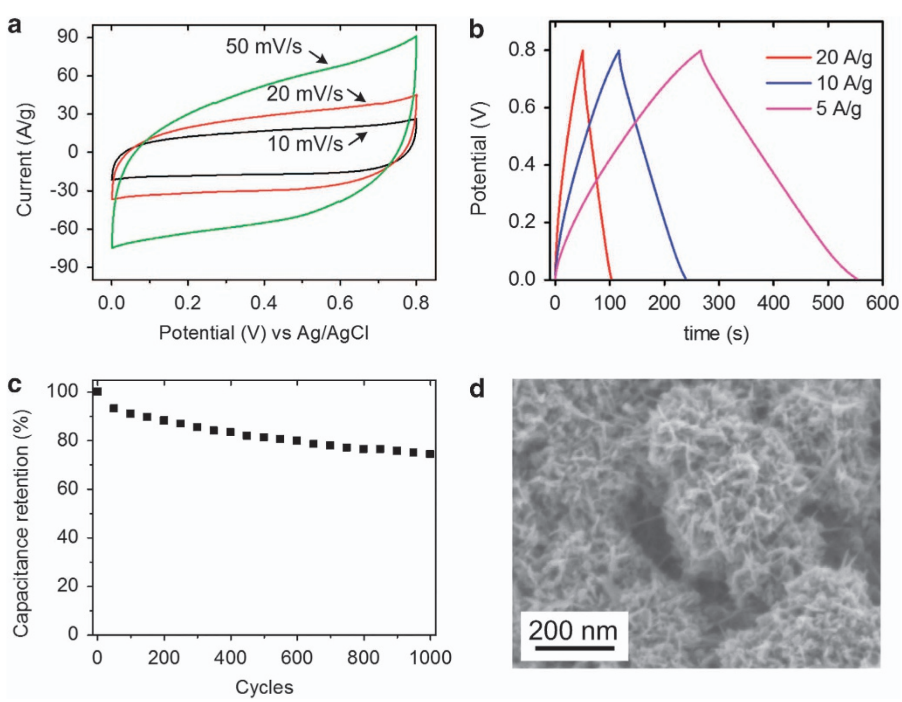

Figure 5 (**a**) Cyclic voltammetry (CV) curves of MnO_x/CNT/RGO nanohybrid at scan rates of 10, 20 and 50 $mV\,s^{-1}$. (**b**) Charge/discharge curves of MnO_x/CNT/RGO nanohybrid at current densities of 5, 10 and 20 $A\,g^{-1}$. (**c**) The capacitance retention of the MnO_x/CNT/RGO nanohybrid is 74% after 1000 cycles at 100 $mV\,s^{-1}$. (**d**) SEM image of MnO_x nanoparticles after cycling.

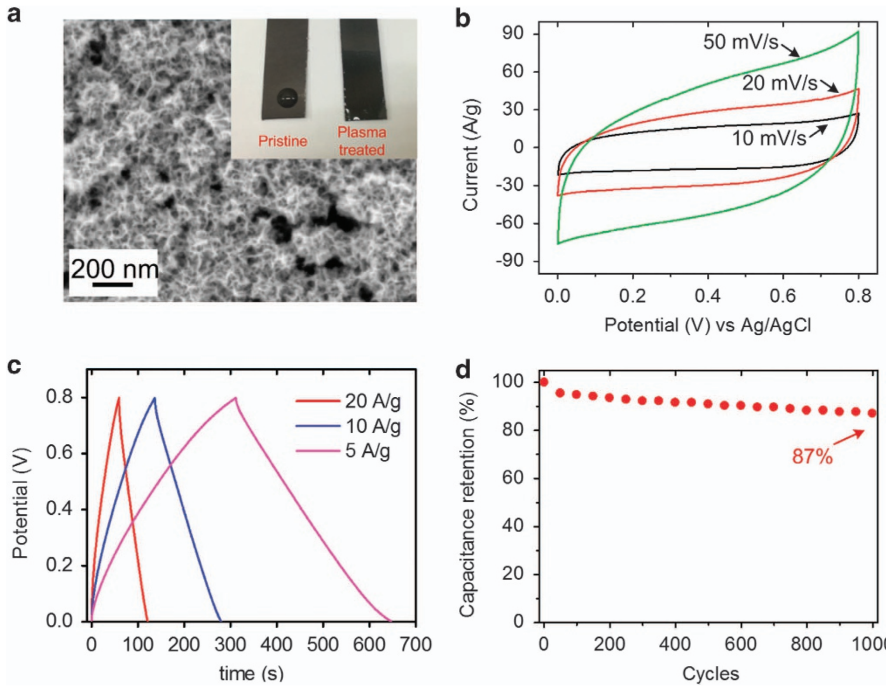

Figure 6 (**a**) SEM image of MnO_x nanoparticles electrodeposited on a plasma-treated CNT/RGO surface. The inset is a photo of CNT/RGO surfaces that shows the wettability change before and after plasma treatment. (**b**) Cyclic voltammetry (CV) curves of MnO_x/CNT/RGO nanohybrid with plasma treatment at scan rates of 10, 20 and 50 mV s^{-1}. (**c**) Charge/discharge curves of MnO_x/CNT/RGO nanohybrid with plasma treatment at current densities of 5, 10 and 20 A g^{-1}. (**d**) The capacitance retention of MnO_x/CNT/RGO nanohybrid with plasma treatment is 87% after 1000 cycles at 100 mV s^{-1}.

Figure 5b shows the galvanostatic charge/discharge curves at current densities of 5, 10 and 20 A g^{-1} (based on the mass loading of MnO_x). The nearly symmetric quasi-triangular shapes of charge/discharge curves again indicate the high and reversible charge storage capacity of the nanohybrid.[25] The specific capacitance C_s of MnO_x/CNT/RGO is calculated to be ~1070 F g^{-1} from the CV curve at a scan rate of 10 mV s^{-1} and ~1040 F g^{-1} from the charge/discharge curve at a constant current of 5 A g^{-1} (both excluding the capacitance of graphite foil). Notably, the specific capacitance remains at a high value of 533 F g^{-1} at a fast scan rate of 100 mV s^{-1}.

The above specific capacitance is substantially higher than those reported for single-phased MnO_2, Mn_2O_3 or Mn_3O_4 materials (~100–300 F g^{-1}) at a similar loading amount (see detailed comparison in Supplementary Table S1).[27,28] This capacitance value also approaches the highest values (900–1170 F g^{-1}) ever reported for hybrid structures, which were obtained either from the very low mass-loading (<10 μg cm^{-2}) of active materials or with a sophisticated current collector (such as nanoporous gold thin films).[26,28,29] In fact, this value (1070 F g^{-1}) is close to the theoretical capacitance of MnO_x (C_s ~ 1240 F g^{-1}) by assuming that all Mn atoms are involved in the redox reactions.

We attribute the high electrochemical performance to the open and nanoporous architecture of the nanohybrid, high electrical conductivity of the CNT/RGO supporting layer and high capacity of the MnO_x compound. Specifically, the porous and flower-like structure could provide a large and accessible surface area to greatly enhance surface ion adsorption, improve the accessibility of cations and shorten the ion diffusion path.[2,17] The smaller and uniformly sized nanoparticles could also facilitate fast charge transfer on the surface or sub-surface of the active material; for example, *Duay et al.*[12] found that the specific capacitance was much higher for small MnO_2 nanofibrils (5–10 nm) than for large MnO_2 nanowires (4.5 μm). In addition, although MnO_x could be gradually oxidized to a higher valent state during the charge/discharge process, the structural features associated with the as-prepared MnO_x, such as ionic (e.g., vacancies and misplaced ions) and electronic (electrons and holes) defects and mismatches at different phases, could still be preserved because of the slow and mild nature of the process.[14] The use of MnO_x nanoparticles as the starting material is thus advantageous compared with the use of MnO_2 for obtaining a higher specific capacitance.

The specific capacitance of the nanohybrid reduces from 1070 to 480 F g^{-1} at 10 mV s^{-1} when the thickness of MnO_x increases from ~200 nm to ~1.2 μm (see Supplementary Figure S12). The relationship between specific capacitance and MnO_x thickness is also plotted based on galvanostatic charge/discharge curves at a high current density of 5 A g^{-1} (see Supplementary Figure S13). These values are notably higher than those obtained from MnO_2-based electrodes and a range of carbon/metal oxide hybrids with similar thicknesses (see Supplementary Table S1). Owing to its higher packing density, the areal capacitance of the thick MnO_x is ~144 mF cm^{-2}, much larger than that of commercial supercapacitors made of activated carbons (~20 mF cm^{-2}).[1] To reasonably translate the measured value to real devices, the loading mass of active materials should generally exceed 1 mg cm^{-2}, and the thickness should be larger than 1 μm.[30] Because one of our aims is evaluation of the ultimate electrochemical performance of MnO_x nanoparticles and demonstration of their potential for energy storage applications, we tried to avoid the effects of intrinsically poor conductivity and impaired ionic accessibility in the excessively thick MnO_x films.[27] Thus, the nanohybrid with a monolayer of MnO_x on the CNT/RGO supporting layer was tested. We emphasize that the fabrication process of single-layer MnO_x/CNT/RGO nanohybrid is simple, fast and non-hazardous, and the thickness of MnO_x can be easily controlled. In the future, the fabrication of multiple-layer MnO_x/CNT/RGO nanohybrids using spray and electrodeposition techniques will also be explored to increase charge storage capacity (see Supplementary Figures S14 and S15).

Improved cyclic stability through plasma treatment

The cycling stability of MnO_x/CNT/RGO is plotted in Figure 5c, showing a relatively poor capacitance retention of ~74% after 1000 cycles at a scan rate of 100 mV s^{-1}. The scanning electron microscopy image of MnO_x nanoparticles after cycling is shown in Figure 5d, in which blunt branches of nanoparticles are observed compared towith the structure before cycling (Figure 1d). This relatively poor cycling stability is most likely due to the dissolution of Mn atoms into the electrolyte and/or the structural instability caused by the adsorption of cations in the redox reactions.[29] A closer investigation of the electrode after cycling also found that a few flake-shaped nanosheets emerge after cycling (see Supplementary Figure S16), indicating that the structure may be affected by the 'dissolution-redeposition' process.[31] The mechanism of this process assumes that Mn atoms at the surface are first dissolved in the electrolyte during reduction at low potentials; the dissolved Mn are then re-oxidized into insoluble MnO_2 and deposit on the surface. The shape of the re-deposited MnO_2 can be very different from that of the original as-prepared MnO_x. As very few flake-shaped nanosheets are found, we conclude that this 'dissolution-redeposition' process is quite slow in the present MnO_x/CNT/RGO nanohybrid. In addition, the XPS spectrum of the cycled electrode shows that Na and S atoms are present in the nanohybrid in addition to the original C, O and Mn atoms (see Supplementary Figure S17), implying that ions in the aqueous electrolyte can intercalate into the active MnO_x structure and cause structural alternations. These effects can thus account for the observed reduced charge storage capacity.

To improve the cyclic stability of the MnO_x/CNT/RGO nanohybrid, we utilized an atmospheric-pressure DBD plasma to functionalize the CNT/RGO supporting layer prior to MnO_x electrodeposition. Plasmas have recently shown a unique ability to selectively functionalize the surface of carbon-based materials with controllable and graded intensity and depth.[32,33] In particular, the low-energy ions and electrons in atmospheric-pressure DBD plasma may be ideal for grafting a variety of functional groups at the outmost regions over a large area without damaging the structure.

We have found that atmospheric-pressure DBD plasma treatment can lead to a notable change in the surface wettability of the CNT/RGO supporting layer after only 15 s of plasma exposure. As the gas temperature is low in the plasma, we were also able to extend the treatment for a much longer time of 5 min to render a more profound plasma modification effect without damaging the structure of the CNT/RGO supporting layer. As shown in the inset of Figure 6a, an almost complete wetting is observed in the plasma-treated CNT/RGO surface, in contrast to the large contact angle of the pristine sample. XPS analyses of the plasma-treated CNT/RGO confirm that substantial numbers of oxygen-containing functional groups, such as −OH and –COOH, are successfully grafted on the surface (see Supplementary Figure S18). Figure 6a also shows an scanning electron microscopy image of MnO_x deposited on a plasma-treated CNT/RGO layer. No apparent difference in the density and morphology is observed compared with the nanoparticles deposited on a pristine CNT/RGO layer; again, flower-like MnO_x nanoparticles form on the surface with high porosity after the same galvanostatic deposition. The results are consistent with previous observations that a carbon surface with substantial functional groups can react easily with metal ions to form metal oxide-based compounds.[34]

The electrochemical performance of MnO_x/CNT/RGO with plasma treatment is shown in Figures 6b–d. The CV and charge/discharge curves are clearly similar to those of CNT/RGO/MnO_x without plasma treatment. Thus, the specific capacitance and rate capability remain nearly unchanged (see Supplementary Figure S19). However, the capacitance retention is greatly improved from 74% of the MnO_x/CNT/RGO without plasma treatment to 87% after plasma treatment. The improved stability is comparable or better than that of many manganese oxide-based pseudocapacitors, with a similar morphology at the same test conditions, such as Mn_3O_4 nanoparticles decorated on CNT arrays (77% retention after 1000 cycles)[35] and graphene sheet/MnO_2 (85% retention after 1000 cycles).[36,37] This improved stability can be explained by noting the two main mechanisms for the capacitance degradation of MnO_x-based electrodes, namely, Mn dissolution and mechanical failure.[31] The former is associated with the partial dissolution of MnO_x into the electrolyte, whereas the latter is caused by mechanical failure upon cycling. With plasma treatment, the better wettability of the CNT/RGO layer could lead to better accessibility of Mn ions in the electrodeposition of MnO_x. However, plasma treatment can also provide a substantial number of functional groups as anchoring sites for MnO_x deposition. The stronger binding between MnO_x nanoparticles and the supporting layer thus effectively improves the mechanical stability during redox reactions and leads to higher capacitance retention over a large number of cycles.[38]

We also measured the electrochemical impedance spectra of the graphite foil, MnO_x/CNT/RGO and MnO_x/CNT/RGO with plasma treatment (see Supplementary Figure S20). The vertical lines in the Nyquist plots support the capacitive behavior of all three electrodes at low frequencies. Moreover, the series resistance, as obtained from the intersections of the electrochemical impedance spectroscopy spectra with the real-Z axis at high frequencies,[2] only slightly increases from 2.9 Ω for the graphite foil to 3.1–3.2 Ω for the MnO_x/CNT/RGO nanohybrids. This low series resistance implies a combinational effect of fast charge transfer in the redox reactions, easy accessibility of ions, and high interfacial contact in the MnO_x/CNT/RGO electrodes, which are all desirable features in the operation of supercapacitors.

CONCLUSION

In summary, we have demonstrated high-performance supercapacitor electrodes based on MnO_x/CNT/RGO nanohybrids. With an ultrathin CNT/RGO supporting layer, the size, morphology and thickness of MnO_x nanoparticles are effectively controlled. Detailed analyses reveal that the MnO_x nanoparticles consist of mainly Mn_3O_4 and Mn_2O_3 phases. The MnO_x/CNT/RGO nanohybrids have key structural features, including porous architecture, small and uniform size, and high electrical conductivity, which lead to high charge storage capacity in supercapacitor operations. In addition, atmospheric-pressure DBD plasmas have been utilized to enhance the binding between MnO_x nanoparticles and the CNT/RGO supporting layer, resulting in further enhancement of cycling stability. Our approach of utilizing nano-hybrids and plasma-related effects is therefore highly promising for the development of next-generation energy storage devices for a range of applications critical for a sustainable future.

CONFLICT OF INTEREST

The authors declare no conflict of interest.

ACKNOWLEDGEMENTS

This work is partially supported by the Australian Research Council (ARC) and CSIRO's OCE Science Leadership program. We acknowledge the DECRA and Future Fellowships from the ARC.

1 Frackowiak, E. & Beguin, F. Carbon materials for the electrochemical storage of energy in capacitors. *Carbon* **39**, 937–950 (2001).
2 El-Kady, M. F., Strong, V., Dubin, S. & Kaner, R. B. Laser scribing of high-performance and flexible graphene-based electrochemical capacitors. *Science* **335**, 1326–1330 (2012).
3 Stoller, M. D., Park, S., Zhu, Y., An, J. & Ruoff, R. S. Graphene-based ultracapacitors. *Nano Lett.* **8**, 3498–3502 (2008).
4 Lee, S., Ha, J., Jo, S., Choi, J., Song, T., Park, W. I., Rogers, J. A. & Paik, U. LEGO-like assembly of peelable, deformable components for integrated devices. *NPG Asia Mater* **5**, e66 doi:10.1038/am.2013.51 (2013).
5 Seo, D. H., Yick, S., Han, Z. J., Fang, J. H. & Ostrikov, K. Synergistic fusion of vertical graphene nanosheets and carbon nanotubes for high-performance supercapacitor electrodes. *ChemSusChem* **7**, 2317–2324 (2014).
6 Li, J., Cheng, X., Shashurin, A. & Keidar, M. Review of electrochemical capacitors based on carbon nanotubes and graphene. *Graphene* **1**, 1–13 (2012).
7 Jiang, J., Li, Y., Liu, J., Huang, X., Yuan, C. & Lou, X. W. Recent advances in metal oxide-based electrode architecture design for electrochemical energy storage. *Adv. Mater.* **24**, 5166–5180 (2012).
8 Zhi, M., Xiang, C., Li, J., Li, M. & Wu, N. Nanostructured carbon–metal oxide composite electrodes for supercapacitors: a review. *Nanoscale* **5**, 72–88 (2013).
9 Seo, D. H., Han, Z. J., Kumar, S. & Ostrikov, K. Structure-controlled, vertical graphene-based, binder-free electrodes from plasma-reformed butter enhance supercapacitor performance. *Adv. Energy Mater.* **3**, 1316–1323 (2013).
10 Su, D., Ahn, H.-J. & Wang, G. b-MnO_2 nanorods with exposed tunnel structures as high-performance cathode materials for sodium-ion batteries. *NPG Asia Mater.* **5**, e70 doi:10.1038/am.2013.56 (2013).
11 Liu, J., Cao, G., Yang, Z., Wang, D., Dubois, D., Zhou, X., Graff, G. L., Pederson, L. R. & Zhang, J.-G. Oriented nanostructures for energy conversion and storage. *ChemSusChem* **1**, 676–697 (2008).
12 Duay, J., Sherrill, S. A., Gui, Z., Gillette, E. & Lee, S. B. Self-limiting electrodeposition of hierarchical MnO_2 and $M(OH)_2/MnO_2$ nanofibril/nanowires: mechanism and supercapacitor properties. *ACS Nano* **7**, 1200–1214 (2013).
13 Varma, C. M. Mixed-valence compounds. *Rev. Mod. Phys.* **48**, 219 (1976).
14 Song, M.-K., Cheng, S., Chen, H., Qin, W., Nam, K.-W., Xu, S., Yang, X.-Q., Bongiorno, A., Lee, J., Bai, J., Tyson, T. A., Cho, J. & Liu, M. Anomalous pseudocapacitive behavior of a nanostructured, mixed-valent manganese oxide film for electrical energy storage. *Nano Lett.* **12**, 3483–3490 (2012).
15 Zhang, H., Cao, G., Wang, Z., Yang, Y., Shi, Z. & Gu, Z. Growth of manganese oxide nanoflowers on vertically-aligned carbon nanotube arrays for high-rate electrochemical capacitive energy storage. *Nano Lett.* **8**, 2664–2668 (2008).
16 Yu, G., Hu, L., Liu, N., Wang, H., Vosgueritchian, M., Yang, Y., Cui, Y. & Bao, Z. Enhancing the supercapacitor performance of graphene/MnO_2 nanostructured electrodes by conductive wrapping. *Nano Lett.* **11**, 4438–4442 (2011).
17 Wang, Y., Han, Z. J., Yu, S. F., Song, R. R., Song, H. H., Ostrikov, K. & Yang, H. Y. Core-leaf onion-like carbon/MnO_2 hybrid nano-urchins for rechargeable lithium-ion batteries. *Carbon* **64**, 230–236 (2013).
18 Skakalova, V., Vretenar, V., Kopera, L., Kotrusz, P., Mangler, C., Mesko, M., Meyer, J. C. & Hulman, M. Electronic transport in composites of graphite oxide with carbon nanotubes. *Carbon* **72**, 224–232 (2014).
19 Li, Z., Mi, Y., Liu, X., Liu, S., Yang, S. & Wang, J. Flexible graphene/MnO_2 composite papers for supercapacitor electrodes. *J. Mater. Chem.* **21**, 14706–14711 (2011).
20 Chigane, M., Ishikawa, M. & Izaki, M. Preparation of manganese oxide thin films by electrolysis/chemical deposition and electrochromism. *J. Electrochem. Soc.* **148**, D96 (2001).
21 Kim, J.-H., Lee, K. H., Overzet, L. J. & Lee, G. S. Synthesis and electrochemical properties of spin-capable carbon nanotube sheet/MnO_x composites for high-performance energy storage devices. *Nano Lett.* **11**, 2611–2617 (2011).
22 Javed, Q., Wang, F. P., Rafique, M. Y., Toufiq, A. M., Li, Q. S., Mahmood, H. & Khan, W. Diameter-controlled synthesis of a-Mn_2O_3 nanorods and nanowires with enhanced surface morphology and optical properties. *Nanotechnology* **23**, 415603 (2012).
23 Jiang, H., Zhao, T., Yan, C., Ma, J. & Li, C. Hydrothermal synthesis of novel Mn_3O_4 nano-octahedrons with enhanced supercapacitors performances. *Nanoscale* **2**, 2195–2198 (2010).
24 Simon, P. & Gogotsi, Y. Materials for electrochemical capacitors. *Nat. Mater.* **7**, 845–854 (2008).
25 Yang, Y., Ruan, G., Xiang, C., Wang, G. & Tour, J. M. Flexible three-dimensional nanoporous metal-based energy devices. *J. Am. Chem. Soc.* **136**, 6187–6190 (2014).
26 Lang, X., Hirata, A., Fujita, T. & Chen, M. Nanoporous metal/oxide hybrid electrodes for electrochemical supercapacitors. *Nat. Nanotech.* **6**, 232–236 (2011).
27 Kang, J., Hirata, A., Kang, L., Zhang, X., Hou, Y., Chen, L., Li, C., Fujita, T., Akagi, K. & Chen, M. Enhanced supercapacitor performance of MnO_2 by atomic doping. *Angew. Chem. Int. Ed.* **52**, 1664–1667 (2013).
28 Xu, C., Kang, F., Li, B. & Du, H. Recent progress on manganese dioxide based supercapacitors. *J. Mater. Res.* **25**, 1421–1432 (2010).
29 Yan, W., Kim, J. Y., Xing, W., Donavan, K. C., Ayvazian, T. & Penner, R. M. Lithographically patterned gold/manganese dioxide core/shell nanowires for high capacity, high rate, and high cyclability hybrid electrical energy storage. *Chem. Mater.* **24**, 2382–2390 (2012).
30 Gogotsi, Y. & Simon, P. True performance metrics in electrochemical energy storage. *Science* **334**, 917–918 (2011).
31 Wei, W., Cui, X., Chen, W. & Ivey, D. G. Electrochemical cyclability mechanism for MnO_2 electrodes utilized as electrochemical supercapacitors. *J. Power Sources* **186**, 543–550 (2009).
32 Ostrikov, K., Neyts, E. C. & Meyyappan, M. Plasma nanoscience: from nano-solids in plasmas to nano-plasmas in solids. *Adv. Phys* **62**, 113–224 (2013).
33 Yang, H. Y., Han, Z. J., Yu, S. F., Pey, K. L., Ostrikov, K. & Karnik, R. Carbon nanotube membranes with ultrahigh specific adsorption capacity for water desalination and purification. *Nat. Comm.* **4**, 2220 (2013).
34 Lee, H., Dellatore, S. M., Miller, W. M. & Messersmith, P. B. Mussel-inspired surface chemistry for multifunctional coatings. *Science* **318**, 426–430 (2007).
35 Cui, X., Hu, F., Wei, W. & Chen, W. Dense and long carbon nanotube arrays decorated with Mn_3O_4 nanoparticles for electrodes of electrochemical supercapacitors. *Carbon* **49**, 1225–1234 (2011).
36 Chen, S., Zhu, J., Wu, X., Han, Q. & Wang, X. Graphene oxide-MnO_2 nanocomposites for supercapacitors. *ACS Nano* **4**, 2822–2830 (2010).
37 Dong, X., Wang, X., Wang, J., Song, H., Li, X., Wang, L., Chan-Park, M. B., Li, C. M. & Chen, P. Synthesis of a MnO_2–graphene foam hybrid with controlled MnO_2 particle shape and its use as a supercapacitor electrode. *Carbon* **50**, 4865–4870 (2012).
38 Kang, J., Hirata, A., Qiu, H.-J., Chen, L., Ge, X., Fujita, T. & Chen, M. Self-Grown oxy-hydroxide@ nanoporous metal electrode for high-performance supercapacitors. *Adv. Mater.* **26**, 269–272 (2014).

Supplementary Information accompanies the paper on the NPG Asia Materials website (http://www.nature.com/am)